IEEE Journal of Microwaves

Received 6 October 2022; revised 22 December 2022 and 23 January 2023; accepted 28 January 2023.

Digital Object Identifier 10.1109/JMW.2023.3242696

A Conformal Mapping-Based Broadband Method to Extract Propagation Properties of Dielectrics Using Coplanar Waveguides With Air Pockets

SENG LOONG YU (Student Member, IEEE), AND EDUARDO A. ROJAS-NASTRUCCI (Member, IEEE)

(Regular Paper)

Department of Electrical Engineering and Computer Science, Embry-Riddle Aeronautical University, Daytona Beach, FL 32114 USA

CORRESPONDING AUTHOR: Eduardo A. Rojas-Nastrucci (e-mail: rojase1@erau.edu).

This work was supported by the National Science Foundation under Grant 1944599.

ABSTRACT In recent years, advances in material science for high-frequency electronics have generated novel materials that offer superior performance. Additive manufacturing (AM) has expanded the frontiers of microwave material manufacturing going beyond flat geometries and unique properties such as graded permittivity materials. Accurate electromagnetic (EM) material characterization for AM materials remains challenging given the printing volume constraints for manufacturing processes, as traditional EM property extraction techniques often require electrically large samples. Furthermore, loss extraction techniques typically cannot differentiate dielectric and conductor losses in waveguides. This paper presents a novel conformal mapping-based characterization technique using coplanar waveguides (CPW) with air pockets that allows for dielectric permittivity and dielectric loss extraction. The underlying principle of the techniques is to use a set of CPWs with different air slot depths to extract the loss behavior as a function of the slot depth. A new loss-slot rate metric is introduced to decouple the dielectric and conductor losses in the structure. The theoretical foundation of the technique is used to develop a physical-mathematical model for dielectric property extraction that is verified with simulations and experiments for materials with permittivity in the range 2.33–29, and loss tangents of 0.02–0.055. The average error for the equivalent capacitance of the CPW with air pockets (CPW-AP) between the presented model and simulated or measured data is 2.4% for all the studied cases. The experimental confirmation is performed with traditionally manufactured FR-4 and additively manufactured yttria-stabilized zirconia (YSZ) dielectrics up to 10 GHz.

INDEX TERMS Additive manufacturing, laser machining, material characterization, dielectric loss, loss tangent, coplanar waveguide, conformal mapping, partial capacitance approximation.

I. INTRODUCTION

With the evolution of additive manufacturing (AM) of microwave packaging in recent years [1], [2], [3], [4], methods of extracting material properties that may be integrated in the AM-oriented design flow have been studied [5], [6], [7], [8], [9], [10], [11]. AM is revolutionizing the field of microwave circuits and antennas by enabling novel geometries and materials that are not practical to achieve by traditional techniques. However, as manufacturing processes and materials continue to evolve, there are often variations in the dielectric properties among devices manufactured with the same machines and raw materials. Furthermore, traditional material characterization techniques require larger samples than what can be printed with state-of-the-art AM technologies for microwave circuit packaging [12], for a given frequency of operation. Hence, a low-cost and dielectric characterization technique that can be implemented using sub-wavelength-long transmission lines to extract both, electric permittivity and loss tangent, and can be performed on each batch of printed parts allows for better quality control, and more accurate material properties for design purposes.

In [5], dielectric relative permittivities of direct digital manufactured (DDM) materials are extracted by a characterization method solely based on S-parameters measurements of a traditional coplanar waveguide (CPW). As shown in [5], the propagation characteristics may be extracted using two methods described in [13], [14]. Once the attenuation and phase constants are calculated, one may determine the relative permittivity of the samples under test by finding the filling factors of the equivalent multilayer CPW structure. The technique described in [5] was applied to additive manufactured materials [15], and extraction of the permittivity was achieved over a broadband frequency range. However, there are limitations for the techniques used in [5], including that attenuation constant includes all the loss mechanisms, namely: dissipative losses, dielectric losses, and radiation; and discerning among the different losses is not possible without adding other types of measurements such as electric conductivity of the conductive layers. Even if DC conductivity is measured, it does not translate to RF conductivity due to material inhomogeneity and considerable surface roughness for conductors.

Another well-known dielectric characterization technique is based on the behavior of resonant cavities. In these techniques, both the permittivity and loss tangent can be accurately extracted by measuring the behavior of the resonator at its resonance frequencies [16], [17], [18]. However, this technique also has limitations, including: (a) the samples to be characterized require a specific shape and dimension to allow insertion in the resonator and accurate measurements and additive manufacturing techniques often are unable to achieve the required dimensions [16]. (b) The extraction technique is only accurate for a range of permittivities and loss tangent values, often for the low-loss ($\tan\delta < 0.01$) and low permittivity ($\epsilon_r < 20$) [17], or otherwise the resonator behavior does not yield accurate results. (c) The material parameters are extracted at discrete frequencies [18].

In this article, a novel conformal mapping-based dielectric permittivity and loss tangent measurement technique is presented. The technique is based on S-parameters measurements of CPW with air pockets (CPW-AP). In typical AM design flow, process control samples are fabricated to characterize the fabrication process and materials to tune the process parameters. This paper proposes fabricating a set of CPW-APs as part of the process control samples on a DDM platform that can be used to extract the electric permittivity and loss tangent of the material, as shown in Fig. 1. Conductive ink is dispensed onto additively manufactured dielectric substrates and a laser machining process is used to create the air pockets. The underlying theoretical base of the technique is studied by first approximating the capacitance. The approximation transforms the structure into the traditional CPW structure and conformal mapping techniques can be applied. Conformal mapping techniques have been recently applied in the additive manufacturing context to model non-uniform conductors due to laser machining processing [1] and meshed ground CPW [2].

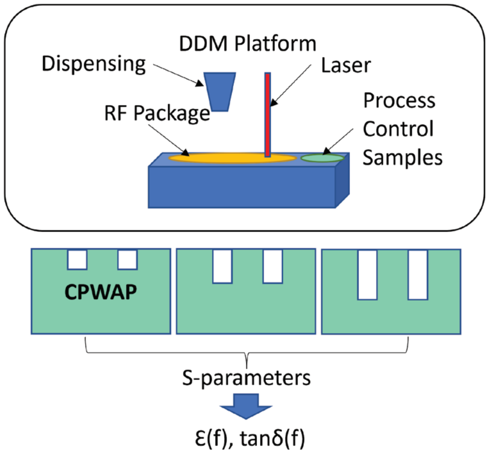

FIGURE 1. Overall dielectric property extraction process using direct digital manufacturing (DDM) platform.

Then, a single-layer reduction approach in [19] is applied to model dielectric losses for such a structure. The goal is to incorporate this material characterization technique in rapid system prototyping design flow such as laser-enhanced direct print additive manufacturing (LE-DPAM), highlighted in [1], [3], [4], to quickly extract unknown microwave material properties.

The physical-mathematical model developed is applied to a wide range of materials ranging in relative permittivity values of 2.33–29 and loss tangents of 0.02–0.055 verified with FEM simulators both at static (Ansys Maxwell.R2) and broadband (Ansys HFSS.R2) conditions. The average error between the presented model and simulated data is 2.4% for all studied cases. A new loss-slot rate metric is introduced to decouple conductor loss from dielectric loss, enabling the extraction of dielectric loss tangent of the material under test. The CPW-AP-based extraction technique is then applied commercial FR-4 laminates and an additively manufactured yttria-stabilized zirconia (YSZ) substrate measuring loss tangents of 0.02 and 0.055 respectively.

II. QUASI-STATIC ANALYSIS OF COPLANAR WAVEGUIDES WITH AIR POCKET SLOTS

A. GENERAL APPROACH AND STRUCTURE GEOMETRY

The propagation characteristics of the coplanar waveguide (CPW) with non-magnetic substrates can be fully characterized by the effective electric permittivity of the structure. Well-known equations [20] for characteristic impedance

$$Z_0 = \frac{1}{c\sqrt{\epsilon_{\text{eff}}}C_a} \tag{1}$$

and dielectric loss

$$\alpha_d = \frac{\pi}{\lambda_0}\frac{\epsilon_r}{\sqrt{\epsilon_{\text{eff}}}}\frac{\epsilon_{\text{eff}}-1}{\epsilon_r-1}\tan\delta \tag{2}$$

is dependent on the effective permittivity of the structure where

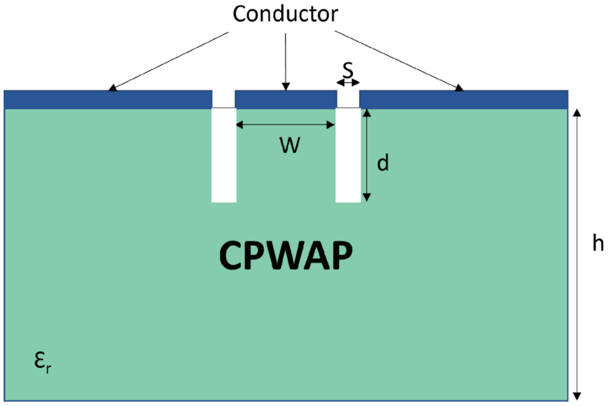

FIGURE 2. Coplanar waveguide with air pocket slots geometry and dimensions.

c = speed of light in vacuum,
ϵ_{eff} = effective permittivity of traveling wave,
C_a = *in-vacuo* capacitance per unit length of the structure,
α_d = attenuation constant due to dielectric losses,
λ_0 = free-space wavelength,
ϵ_r = relative permittivity of CPW substrate,
$\tan\delta$ = loss tangent of CPW dielectric substrate.

The CPW with air pocket slots, as shown in Fig. 2 , is analyzed in this section.

The underlying principle used in the technique is that the contribution of the dielectric losses to the overall losses is a function of the depth of the air pocket slots. When having a set of CPW-AP with different air pockets slots sizes, it is possible to extract the contribution of the dielectric loss tangent to the overall CPW-AP loss, hence, extract its loss tangent.

In addition to having the typical CPW geometry parameters W, S, and h, the structure now includes d, the depth of the slot for the air pockets. Therefore, the study of slot depth's effect on the effective permittivity would result in fully knowing the propagation characteristics of the structure of interest. Here, the study without the effect of conductor losses is presented.

B. PARTIAL CAPACITANCE APPROXIMATION OF CPW WITH AIR POCKET SLOTS

Traditional conformal mapping techniques [20] that are applied to traditional CPW geometries are not compatible with CPW-AP. Partial capacitance approximation (PCA) of traditional CPWs is typically calculated by transforming the CPW geometry into a parallel-plate configuration to model the capacitance per unit length of the structure [20] using Schwarz-Christoffel (SC) mapping [21], [22]. SC mapping of the lower-half plane in Fig. 2 to a rectangle would result in the air pocket slots' vertices being mapped within the rectangle, as shown in Fig. 3. Here, the vertices $A, B, \ldots, I, J$ are mapped to $A,' B,' \ldots, I,' J'$, where points $G,' H,' I'$, and J' is anywhere within the rectangle $A'B'C'D'$ depending on the value of slot depth d. The resulting capacitor structure is no longer a homogeneous dielectric medium where the capacitance can be conveniently calculated. Furthermore, numerical analysis would be needed to find the vertices of the mapped structure. The resulting conformal map directly from the CPW-AP geometry does not lead to a geometry with field lines that follow the traditional parallel plate field distribution. However, it is possible to approximate the capacitance per unit length of Fig. 2 by splitting the structure into three different regions and analyzing the structure as a multilayer CPW as shown in Fig. 4. Using [20] to find the total capacitance of a multilayer CPW yields

$$C_{\text{CPW}} = 2C_1 + C_2 - C_{\text{slot}} \tag{3}$$

where C_1 is the capacitance in air (Fig. 4a), C_2 is the capacitance in dielectric $\epsilon_r - 1$ (Fig. 4b), and C_{slot} is the slot capacitance with permittivity ϵ_r (Fig. 4 c). C_{slot} has dimensions of depth d and slot width S. Since C_{slot} is the capacitance of the slot, the total capacitance in (3) can be approximated by subtracting C_{slot} from the conventional single layer CPW with capacitance $2C_1 + C_2$.

As discussed earlier, the electric fields do not retain the property of harmonic functions if transformed using conventional SC mapping. However, by simulation-based experimentation and inspection, it was found that the permittivity of the geometry shown in Fig. 4(c) can be modeled by a homogeneous medium with

$$\epsilon_{r,\text{slot}} = \epsilon_r - \sqrt{\epsilon_r}. \tag{4}$$

The converted structure is shown in Fig. 5.

Using the converted structure in Fig. 5 and from Schwarz-Christoffel mapping of the half-plane into a rectangle to find the partial capacitances yields

$$C_1 = 2\epsilon_0 \frac{K(k_1)}{K(k_1')}, \tag{5}$$

$$C_2 = 2(\epsilon_r - 1)\epsilon_0 \frac{K(k_2)}{K(k_2')}, \tag{6}$$

and

$$C_{\text{slot}} = 2\left(\epsilon_r - \sqrt{\epsilon_r}\right)\epsilon_0 \frac{K(k_s)}{K(k_s')} \tag{7}$$

where

$$k_1 = a/b \tag{8a}$$

$$k_2 = \sinh(\pi a/2\,h)/\sinh(\pi b/2\,h) \tag{8b}$$

$$k_s = \sinh(\pi a/2\,d)/\sinh(\pi b/2\,d). \tag{8c}$$

In (8), $a/b = W/(W + 2S)$ is the aspect ratio of the CPW and h is the height of the dielectric substrate. $K(k_i)$ is the complete elliptic integral of the first kind,

$$K(k_i) = \int_0^{\pi/2} \frac{d\theta}{\sqrt{1 - k_i^2 \sin^2\theta}}, \tag{9}$$

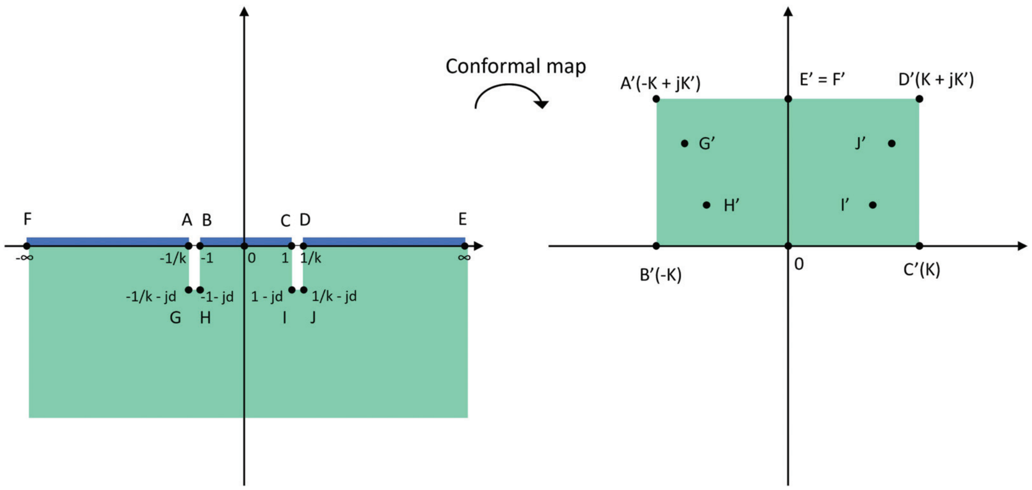

FIGURE 3. Conformal mapping of CPW-AP structure directly using traditional CPW mapping function.

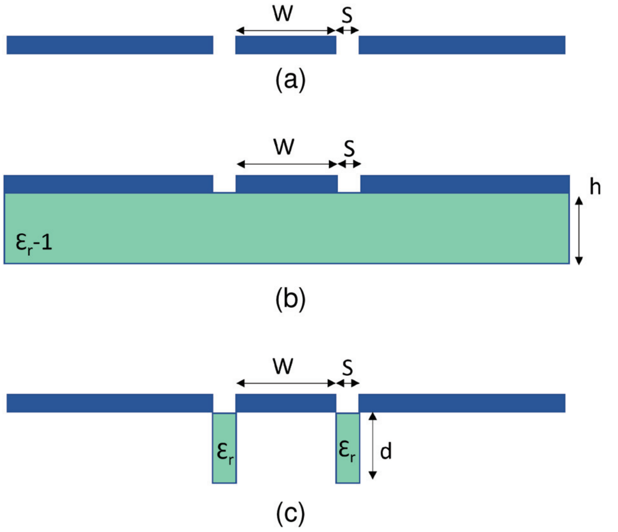

FIGURE 4. Splitting the CPW with air pocket slots structure into three distinguished layers. (a) CPW in air (C_1). (b) CPW on substrate height *h* (C_2). (c) CPW with only slot capacitance (C_{slot}).

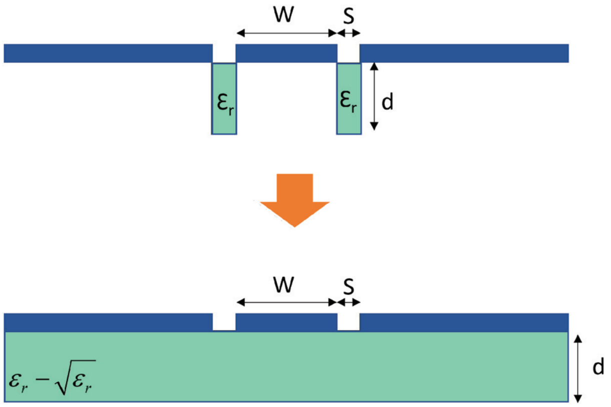

FIGURE 5. Transformation of Fig. 4(c) into a CPW on homogeneous medium with height *d*.

and $k_i' = \sqrt{1-k_i^2}$. Therefore, the effective permittivity can be expressed as

$$\epsilon_{\text{eff}} = \frac{C_{\text{CPW}}}{C_{\text{air}}} = 1 + \frac{\epsilon_r - 1}{2}\frac{K(k_2)}{K(k_2')}\frac{K(k_1')}{K(k_1)} - \frac{\epsilon_r - \sqrt{\epsilon_r}}{2}\frac{K(k_s)}{K(k_s')}\frac{K(k_1')}{K(k_1)} \tag{10}$$

where the capacitance C_{air} is simply $2C_1 = 4\epsilon_0 K(k_1)/K(k_1')$, containing both the upper and bottom halves of the complex plane. One should note when there are no air pocket slots in the CPW, $C_{\text{slot}} \to 0$ since (8c) approaches zero as $d \to 0$:

$$C_{\text{slot}}(d=0) = \lim_{d\to 0}\left[2\left(\epsilon_r - \sqrt{\epsilon_r}\right)\epsilon_0 \frac{K(k_s)}{K(k_s')}\right] = 0 \tag{11}$$

when

$$\lim_{d\to 0} K(k_s) = K\left\{\underbrace{\lim_{d\to 0}\left[\frac{\sinh(\pi a/2\,d)}{\sinh(\pi b/2\,d)}\right]}_{0}\right\} = \frac{\pi}{2} \tag{12}$$

and

$$\lim_{d\to 0} K(k_s') = K\left\{\sqrt{\underbrace{\lim_{d\to 0}\left[1 - \left(\frac{\sinh(\pi a/2\,d)}{\sinh(\pi b/2\,d)}\right)^2\right]}_{1}}\right\} = \infty \tag{13}$$

for $a/b < 1$. The effective permittivity is then equal to the case of the CPW with substrate height h, as studied in [20]:

$$\epsilon_{\text{eff}} = 1 + \frac{\epsilon_r - 1}{2}\frac{K(k_2)}{K(k_2')}\frac{K(k_1')}{K(k_1)}. \tag{14}$$

C. SINGLE-LAYER REDUCTION (SLR) PROCESS

An expression as in (2) is required to show the relationship between the attenuation losses and the relative permittivity

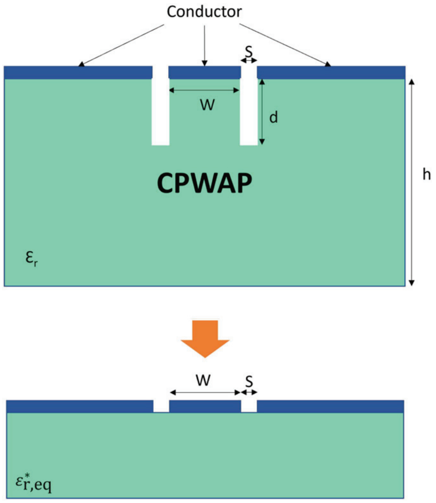

FIGURE 6. Transformation of CPW-AP into equivalent CPW structure on a substrate of infinite height.

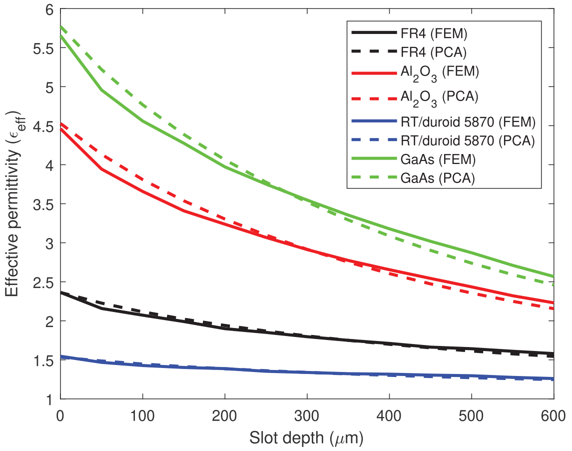

FIGURE 7. Comparison of effective permittivity PCA calculations and FEM simulation.

and loss tangent for CPW-AP. The effective permittivity of the traditional CPW structure in Fig. 2 can be conveniently calculated with (10). (2) cannot be used to directly calculate the attenuation due to dielectric loss since the CPW is not supported on a homogeneous medium such as in Fig. 4(b). Previously, the structure in Fig. 2 was transformed into a multilayer configuration in Fig. 4 with $C_{\text{CPW}} = 2C_1 + C_2 - C_{\text{slot}}$. In [19], it is shown that for multilayer CPW configurations, one can calculate the overall dielectric loss by effectively reducing the CPW in a homogeneous medium with complex permittivity ϵ^*_{eff} into a CPW suspended on homogeneous medium equivalent permittivity $\epsilon_{r,\text{eq}}$ and equivalent loss tangent $\tan\delta_{\text{eq}}$. This transformation is graphically shown in Fig. 6.

The transformation can be carried out by considering the expression for the effective complex permittivity of a CPW suspended on an infinitely thick substrate with $\epsilon^*_{\text{eff}} = 1 + q(\epsilon^*_{r,\text{eq}} - 1)$ [19], where q is the CPW partial filling factor and $\epsilon^*_{r,\text{eq}}$ is the complex equivalent permittivity. Letting $q = 1/2$ for the transformation into the desired structure (a CPW suspended on an infinitely thick substrate) yields

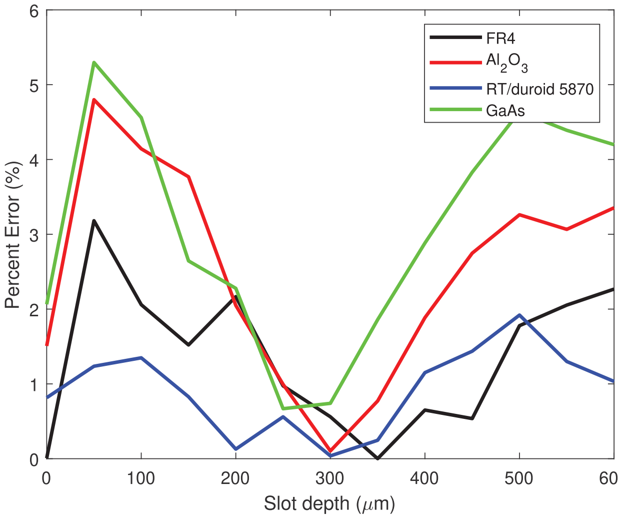

FIGURE 8. Error between PCA calculations and FEM simulation.

$$\epsilon^*_{r,\text{eq}} = 2\epsilon^*_{\text{eff}} - 1. \tag{15}$$

With the expression complex equivalent relative permittivity in (15), the equivalent loss tangent can be calculated with the ratio of the real and imaginary parts of $\epsilon^*_{r,\text{eq}}$:

$$\tan\delta_{\text{eq}} = \left| \frac{\text{Im}\left(\epsilon^*_{r,\text{eq}}\right)}{\text{Re}\left(\epsilon^*_{r,\text{eq}}\right)} \right| \tag{16}$$

Finally, substituting the equivalent relative permittivity and equivalent loss tangent back into (2) yields

$$\alpha_d = \frac{\pi}{\lambda_0} \frac{\epsilon_{r,\text{eq}}}{\sqrt{\epsilon_{\text{eff}}}} \frac{\epsilon_{\text{eff}} - 1}{\epsilon_{r,\text{eq}} - 1} \tan\delta_{\text{eq}}. \tag{17}$$

D. DERIVATIVES OF EXTRACTED PROPAGATION CHARACTERISTICS AND EXTRACTION METHODOLOGY

To quantify dielectric loss without the effects of conductor loss with increasing slot depth, it is useful to consider the loss-slot rate (a partial derivative)

$$\delta_\alpha = \left| \frac{\partial \alpha}{\partial d} \right| \tag{18}$$

where α is the total measured loss of the CPW (including effects of conductor loss) and d is the slot depth. Since the slot depth only affects the fields in the dielectric-air interface, it is possible to use (18) to compare measured samples to ideal simulation models to extract the $\tan\delta$ of the dielectric. As long δ_α is equal for both measurements and simulations, the loss tangent of the material can be extracted using (18) as a metric.

For a CPW line with no air pockets, the measured and simulated attenuation constants contain losses from the conductor and dielectrics. Computing the loss-slot rate (δ_α) decouples the dielectric effects from the conductor losses, hence providing a way to accurately extract the contribution to losses by the dielectric ($\tan\delta$).

For example, hypothetical loss-slot rate (δ_α vs. d) curves for different loss tangents are generated using EM simulation. Since δ_α decouples the conductor loss from the total losses, the measured δ_α will closely match of one the generated EM simulated curves. The matching of the measured and simulated δ_α allows the extraction of $\tan\delta$. This process is later demonstrated in Section V.

III. VALIDATION OF MATHEMETICAL MODELS USING EM SIMULATIONS

A. COMPARISON OF PCA MODEL AND FEM EM SIMULATIONS

To verify the partial capacitance approximation shown previously, theoretical PCA calculations are compared to FEM simulations of the structures with varying slot depth d. The FEM simulator used is Ansys Maxwell 2021.R2, where the capacitance of the CPW in Fig. 2 is extracted and divided by the capacitance of the CPW with the same aspect ratio suspended in air, as in Fig. 4(a). In the calculations and simulations, the CPW has the geometry of $W = 1$ mm, $S = 0.5$ mm, and $h = 0.813$ mm where the slot depth d is the variable being swept. To ensure that the approximation is valid for materials with varying dielectric constants, a wide variety of dielectrics were considered in this comparison.

As shown in Fig. 7, the dielectrics used in the comparison were FR-4, alumina (Al_2O_3), RT/duroid 5870, and gallium arsenide (GaAs) with ϵ_r of 4.4, 9.8, 2.33, and 12.9 respectively. In all cases, the effective permittivity reduces as the slot depth is increased, this is expected since the air pockets effectively reduce the area of the dielectric. It is especially prevalent with materials of higher permittivity, as in the case of alumina and gallium arsenide.

Accompanied by the comparison, an error plot Fig. 8 is generated to monitor the deviation that the approximation may have caused. As seen, the error is less than 5.5% in all cases, up to etching - with a slot depth down to 75% of the substrate height.

To verify the mathematical model for a wide range of CPW aspect ratios, where $a/b = W/(W + 2S)$, Fig. 9 shows the simulated relative permittivities while Fig. 10 shows the calculated values using the described mathematical model. As shown in Fig. 11, the error is less than 5% for $0.3 \le a/b \le 0.7$ and up to 10% for more extreme a/b values in the range of $0.2 \le a/b \le 0.8$.

Furthermore, the phase constant β is expected to change since $\beta = 2\pi/\lambda_g$ where $\lambda_g = c/(\sqrt{\epsilon_{\text{eff}}} f)$ is the guided wavelength and c is the speed of light in vacuum. This will cause the phase response zero-crossings of S_{21} to shift toward the right when the slot depth d is increased. A FEM simulation is created to verify this as shown in Fig. 12. The CPW structure is simulated in Ansys HFSS 2021.R2 with the same dimensions as the case in Fig. 7 with FR-4 ($\epsilon_r = 4.4$) selected as the material with a physical length of $L = 20$ mm. It is seen that the phase zero-crossings shift right in both cases as the slot depth increases, verifying the hypothesis.

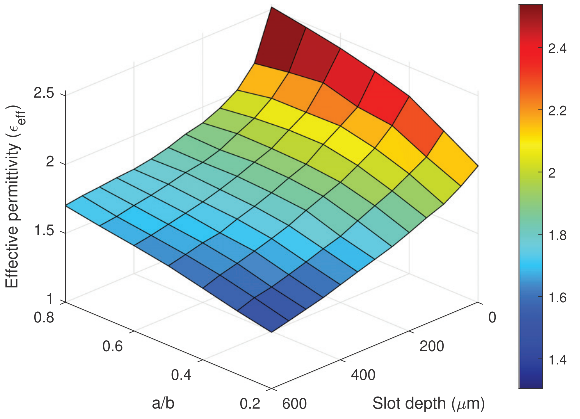

FIGURE 9. Simulation of CPW effective permittivity for various slot depths and a/b ratios on FR-4.

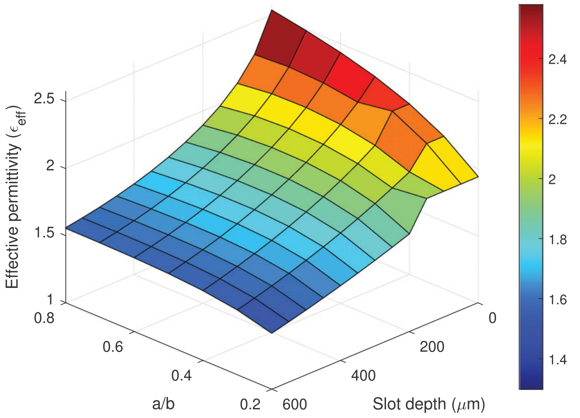

FIGURE 10. Mathematical model of CPW effective permittivity for various slot depths and a/b ratios on FR-4.

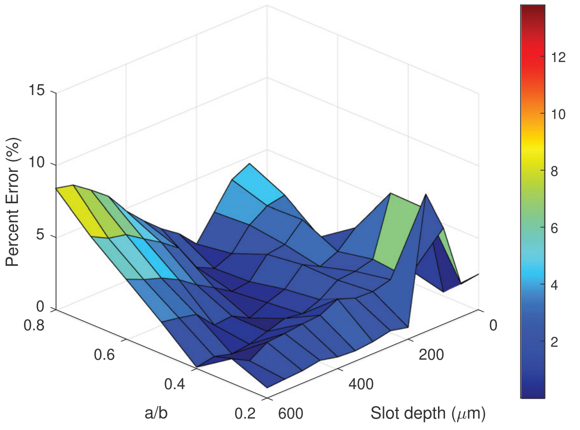

FIGURE 11. Error between PCA calculations and FEM simulation.

B. COMPARISON OF SLR PROCESS ON CPW-AP AND FEM EM SIMULATIONS

To verify the analytical approach using PCA and SLR, a comparison of the calculated parameters is done against a FEM simulation on FR-4 material with $\epsilon_r = 4.4$ and $\tan\delta = 0.02$.

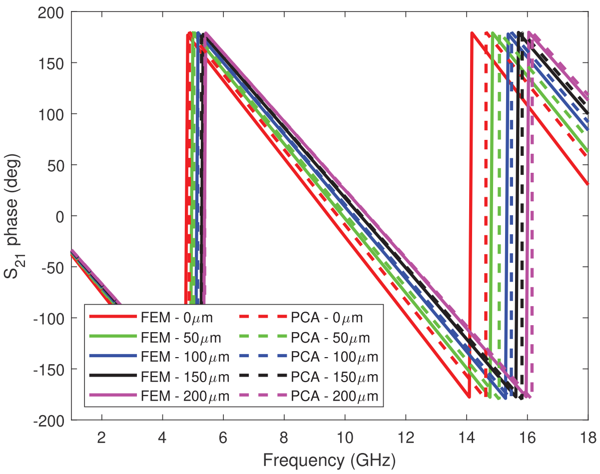

FIGURE 12. **Comparison of calculated and simulated S_{21} phase of CPW at various depth d.**

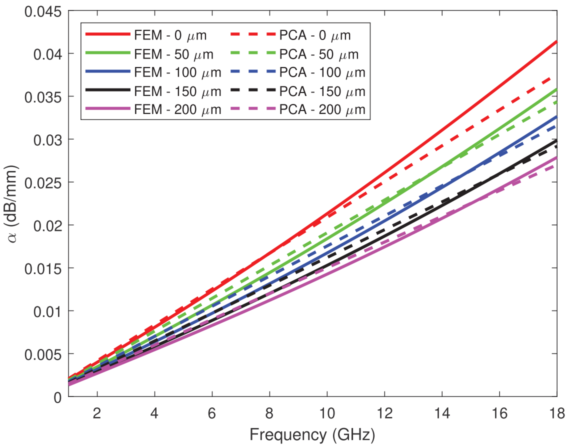

FIGURE 13. **Comparison of calculated and simulated dielectric loss of CPW at various depth d.**

Ansys HFSS 2021.R2 is used to find the attenuation constant purely from dielectric loss by letting the conductor be a sheet of perfect electrical conductor (PEC). For the theoretical and simulated CPW structure, the parameters are $W = 1$ mm, $S = 0.5$ mm, $L = 20$ mm, and $h = 0.813$ mm. A frequency sweep of the attenuation constant α is generated for $d = 0$ μm to $d = 200$ μm in steps of 50 μm up to 18 GHz. This comparison is shown in Fig. 13.

As seen in Fig. 13, the calculated and simulated attenuation due to dielectric loss is comparable in magnitude, especially at high frequencies. In HFSS simulations, the complex propagation constant γ is calculated by the simulator on the wave port that it is excited, and the attenuation constant α can be found by taking the real part of γ since $\gamma = \alpha + j\beta$. As expected, the loss is reduced by increasing slot depth. This is because ϵ_{eff} dictates the loss in (17).

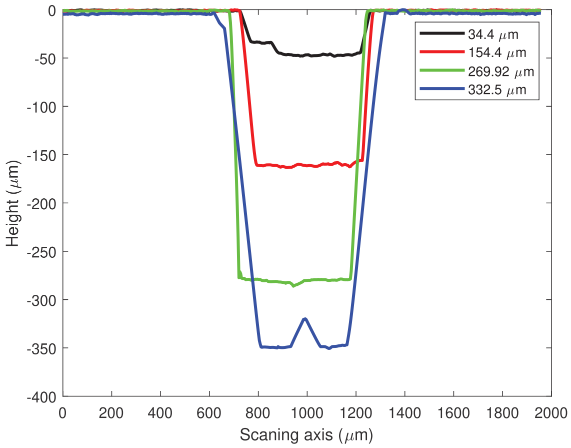

FIGURE 14. **Profile height measurements of fabricated CPW samples on FR-4 substrate. The labeled depths shown exclude the thickness of copper.**

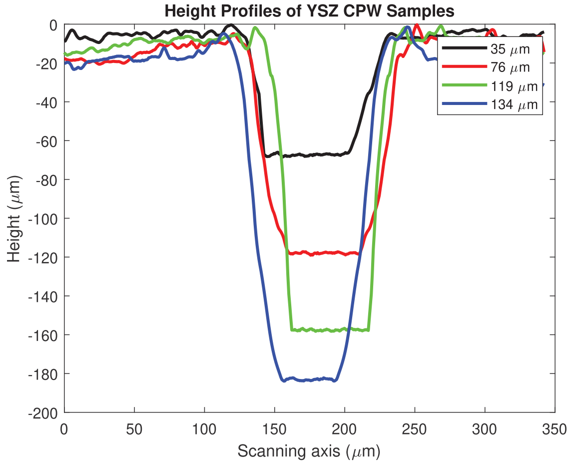

FIGURE 15. **Profile height measurements of fabricated CPW samples on YSZ substrate. The labeled depths shown exclude the thickness of deposited CB028.**

IV. EXPERIMENTAL VERIFICATION OF THE CPW-AP TECHNIQUE

A. FABRICATION

Samples of the CPW with air pockets slots are fabricated on FR-4 since the dielectric loss is comparably high for measurement convenience. The CPW geometrical parameters are $W = 1$ mm, $S = 0.5$ mm, $L = 20$ mm, and $h = 0.813$ mm. The samples were fabricated using the LPKF ProtoMat S103 milling machine. To etch out material for the air pockets, a 2.5D process was added into the fabrication process where it is possible to remove material up to 300 μm deep from the surface.

Furthermore, a set of additively manufactured dielectric substrate with unknown dielectric loss was used to demonstrate the methodology. These samples were fabricated on a yttria-stabilized zirconia (YSZ) substrate, additively manufactured using digital light processing (DLP) technology. The CPW has the geometrical parameters of $W = 0.3$ mm, $S = 0.1$ mm, $L = 3$ mm, and $h = 1.81$ mm. The slurry AdmaPrint

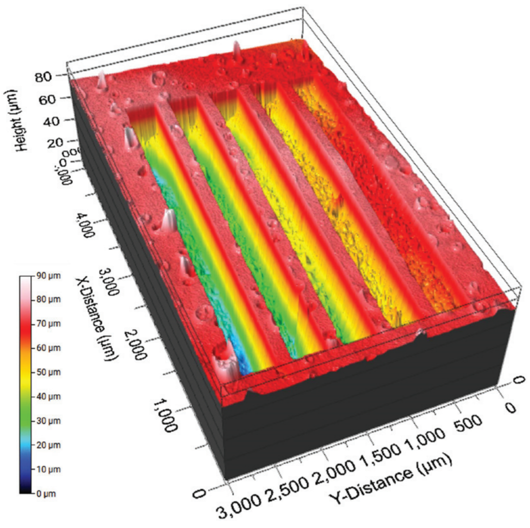

FIGURE 16. **3-D profile height measurements of an array of laser machined slots. The substrate is not entirely flat due to production errors.**

Z130 was used to create the substrates. After printing and sintering, the substrate is measured to have a height of 1.81 mm. Then, DuPont CB028 was micro-dispensed using the nScrypt 3Dn Tabletop on the YSZ surface to create the CPW conductors. Finally, the CPW slots and air pockets are etched by a Spark Lasers DIADEM 1064-10 compact high-energy femtosecond laser with a Thorlabs LMH-20X-1064 high-power focusing 20× objective. The laser machining process uses a peak power of 1 MW, laser path speed of 50 mm/s, repetition rate of 10 kHz, and pulse width of 360 fs. To create the different slot depths, the number of passes of the laser path is varied accordingly, at 5, 10, 15, and 20 for a total of four samples.

The height profiles of the fabricated FR-4 samples are shown in Fig. 14. Surface profiles are measured with a Filmetrics Profilm3D profilometer. As shown, the air pocket slots have depths of 35.4 μm, 254.4 μm, 269.92 μm, and 332.5 μm respectively, obtained by subtracting the thickness of copper of 17.5 μm. Similarly, the YSZ samples are shown in Fig. 15. Here, the air pocket slots have depths of 35 μm, 76 μm, 119 μm, and 134 μm respectively, obtained by subtracting the thickness of cured CB028 ink of 30 μm. A 3-D profile is shown in Fig. 16 for an array of slots used to characterize the laser machining parameters for the YSZ substrate. In Fig. 16, the leftmost cut is 5 passes while the rightmost cut has only 1 pass. In this array, the laser machining process uses a peak power of 1 MW, laser path speed of 50 mm/s, repetition rate of 10 kHz, and pulse width of 360 fs.

B. MEASUREMENTS OF SAMPLES

S-parameters measurements of the FR-4 samples were then taken on the Keysight N5227B PNA Network Analyzer with GGB 40A-GSG-1250-DP Picoprobes and SOLT calibration was performed with the CS-10 calibration kit. To verify that the effective permittivity is changing with air pocket slots, the phase of S_{21} is measured and compared to the simulation as shown in Fig. 17. As discussed previously, it is expected that the zero-crossings of the transmission phase to shift to higher frequencies, due to the decrease in effective permittivity. The measurements are in agreement with this hypothesized behavior.

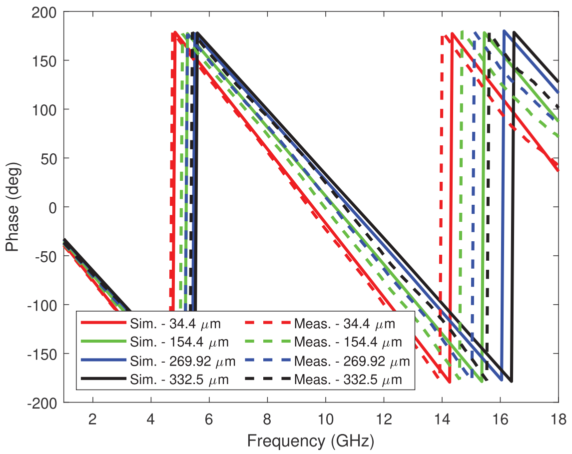

FIGURE 17. **Comparison of simulated and measured S_{21} phase of fabricated samples.**

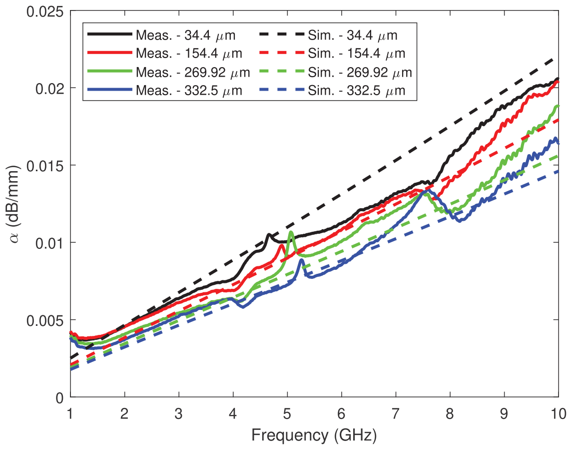

FIGURE 18. **Comparison of simulated and measured attenuation constant of fabricated FR-4 samples.**

Furthermore, the extracted attenuation constant α through the methodology in [5] is compared to the FEM simulations. However, the effects of conductor loss are considered in this comparison with copper thickness $t = 18$ μm and electrical conductivity $\sigma = 5.8 \times 10^7$ S/m. This is shown in Fig. 18 where α is extracted up to 10 GHz. It is shown that the overall loss is decreased as slot depth is increased, which confirms the hypothesis presented at the start. Due to the dynamic range of the network analyzer, the effects from measurements are only noticeable at higher frequencies.

A similar approach was taken for the YSZ samples. Since the samples are smaller and due to the high permittivity of YSZ ($\epsilon_r = 29$), a TRL calibration was performed on the Keysight N5227B PNA Network Analyzer with GGB

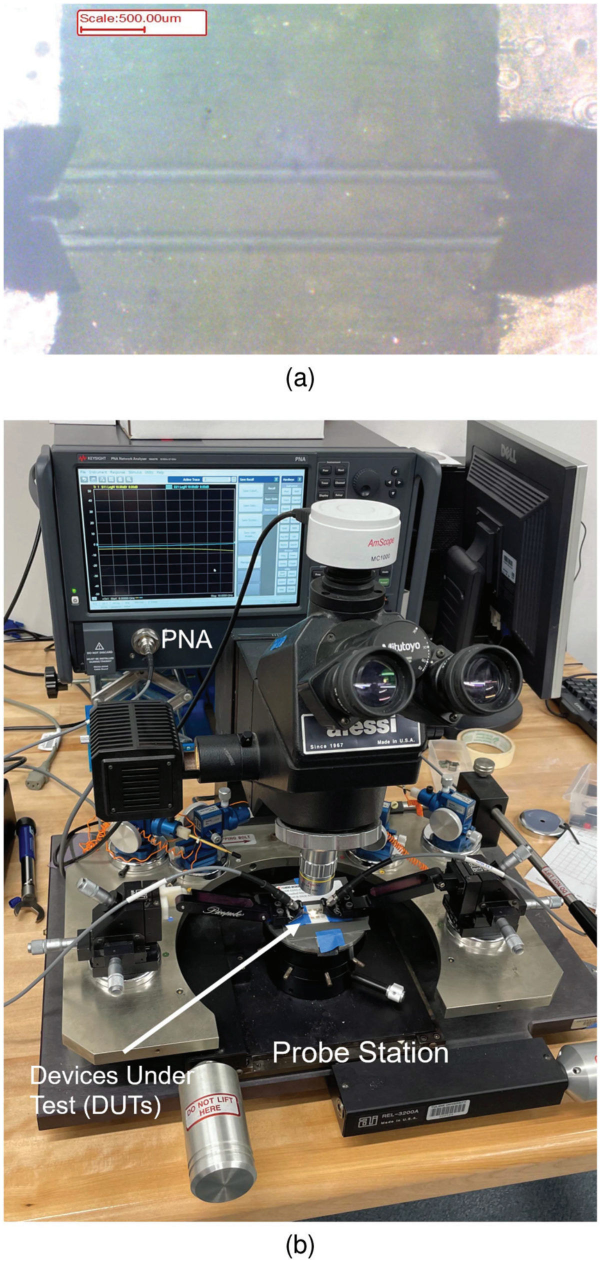

(a)

(b)

FIGURE 19. **(a) Optical image of probed YSZ sample. (b) Measurement equipment and setup for YSZ samples.**

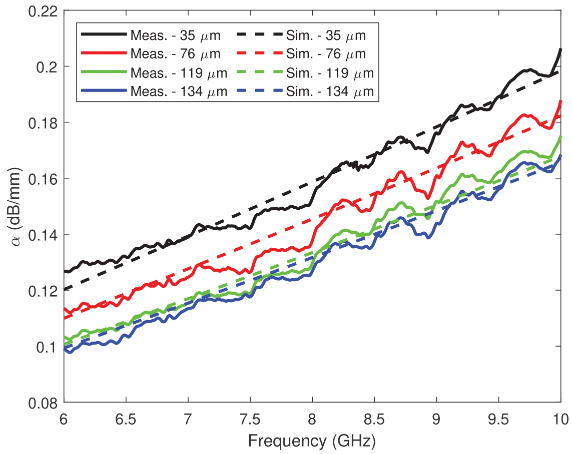

FIGURE 20. **Comparison of simulated and measured attenuation constant of fabricated YSZ samples.**

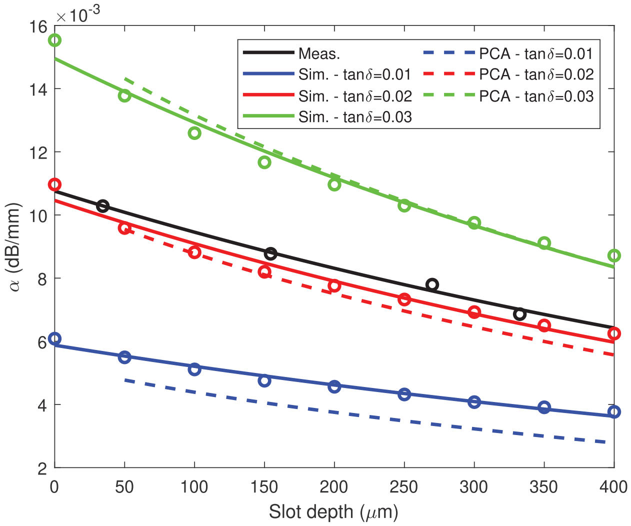

FIGURE 21. **Attenuation constant versus slot depth curves for FR-4 at 6 GHz. The curves are fitted with an exponential curve of the form $y = ae^{bx}$.**

40A-GSG-600-DP Picoprobes and calibrated with the CS-9 calibration kit to achieve more stable S_{21} phase responses across the YSZ CPW samples. Hence, the calibration for the YSZ samples is performed in the range 6 GHz–10 GHz, the measurement setup is shown in Fig. 19. In Fig. 20, the attenuation constant is extracted and compared with the FEM simulation with silver thickness $t = 30\ \mu$m and electrical conductivity $\sigma = 2 \times 10^7$ S/m.

V. RESULTS AND DISCUSSION

Based on the proposed $\tan\delta$ extraction technique, it is possible to plot the attenuation constant α at any frequency and fit the curve through an exponential curve as shown in Fig. 21. Fig. 7 suggests that ϵ_{eff} reduces approximately exponentially as slot depth d increases, thus an exponential function is used for curve fitting. Besides the measurements, FEM simulations are obtained for various loss tangents. In Fig. 21, several α versus d curves for hypothetical loss tangent values of FR-4, namely 0.01, 0.02, and 0.03, are generated with $\epsilon_r = 4.4$ and $\sigma = 5.8 \times 10^7$ S/m.

It is also seen that in Fig. 21, the measurements do not line up with any of the loss tangent curves. As stated before the total losses in the measurements contains unknown effects such as conductor loss, surface roughness, radiation, etc. By evaluating (18) for the different loss tangent values and the curve-fitted measurements, it is seen that the measurements are most aligned with the δ_α for when $\tan\delta = 0.02$, as shown in Fig. 23.

Similarly, the same process was applied to the unknown YSZ samples. First, the α versus d curves for hypothetical

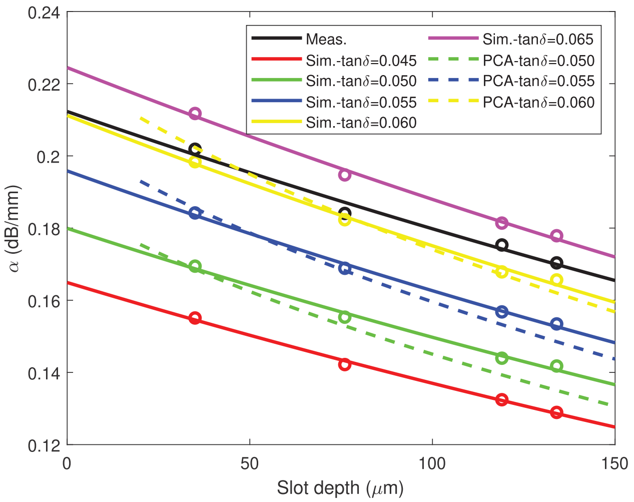

FIGURE 22. **Attenuation constant versus slot depth curves for YSZ at 10 GHz. The curves are fitted with an exponential curve of the form $y = ae^{bx}$.**

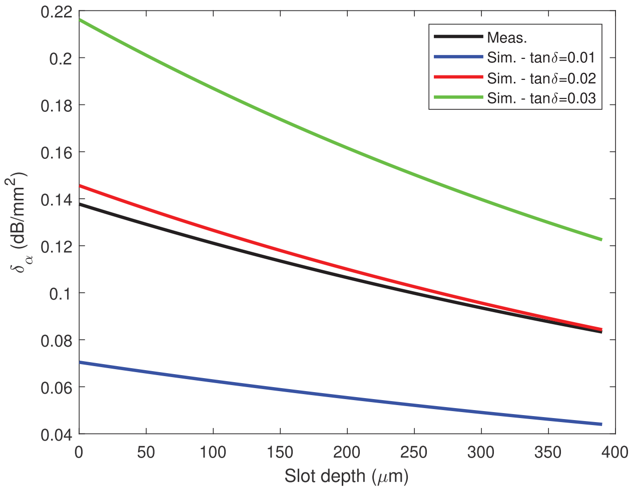

FIGURE 23. **δ_α curves generated from simulation and measurements for FR-4 at 6 GHz.**

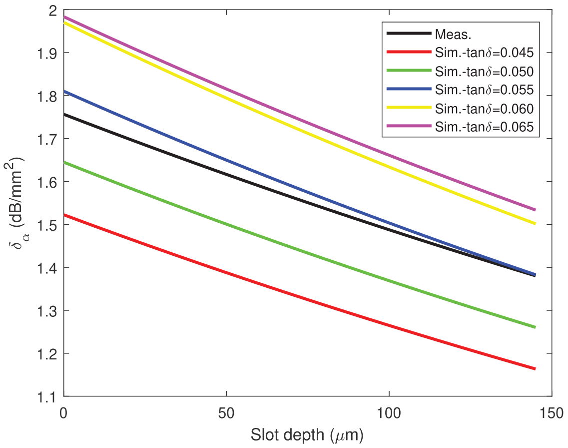

FIGURE 24. **δ_α curves generated from simulation and measurements for YSZ at 10 GHz.**

loss tangents of 0.045, 0.05, 0.055, 0.06, and 0.065 are generated in HFSS with $\epsilon_r = 29$ and $\sigma = 2 \times 10^7$ S/m. Then, the numerical derivative is computed and shown in Fig. 24. Here, the measured δ_α curve lies closest to the $\tan\delta = 0.055$ curve, suggesting that the fabricated YSZ sample has a loss tangent of 0.055. Additionally, the PCA/SLR model is included in Fig. 21 and Fig. 22 to further support the mathematical modeling of CPW-AP in the previous section. Alternative methods using the PCA model may be used, but it is still advised to use accurate FEM EM simulations to avoid large discrepancies in calculated results, as errors up to 10% may be incurred as shown in Fig. 11 depending on structure geometry and material used.

With this characterization methodology, it is possible to extract the loss tangent of materials by creating CPW samples with varying air pocket slots. As shown in Fig. 23, evaluating (18) is sufficient since the effects of surface roughness or conductor loss is negligible with the partial derivative.

VI. CONCLUSION

It is shown that for CPW structures with air pocket slots, the effective permittivity is decreased as the slot depth is increased. This causes characteristic impedance and propagation constant changes for an over-etched CPW. The phenomena are analyzed using a partial capacitance approximation technique, this allowed a quick and also accurate method to model its propagation characteristics. Errors between simulated and measured results are less than 10% across all the studied material and geometries. To describe its effect on the dielectric loss, the single layer reduction (SLR) method proposed by [19] is used to calculate the dielectric loss. Again, the approximations and calculations agree with FEM simulations. Experimental data is also used to verify the effect of the air pocket slots on propagation characteristics. The discussion included its effect on both the effective permittivity and dielectric loss. Finally, it is shown that the structure can be utilized to extract the loss tangent of unknown materials by introducing a new loss-slot rate (δ_α) metric in the form of (18). It is shown that in an example the loss tangent for FR-4 is extracted to be 0.02, which agrees with manufacturer data [23]. The methodology is also applied to an additive-manufactured YSZ sample with unknown RF characteristics and was shown to have a $\tan\delta$ of 0.055. This extraction methodology and the combination of [5] can be integrated to an additive manufacturing design process to quickly characterize unknown materials in an additive manufacturing design flow.

The methodology presented in this article is shown to be convenient in AM processes, in that samples can be created as part of the control process and that material properties can be determined on a batch-by-batch basis. However, it has still room for improvement. For example, dielectric losses can currently only be determined by having a set of loss-slot rate (δ_α vs d) curves through EM simulation, which may be an inconvenience when attempting to characterize a material. A potential recommendation is to leverage machine learning

(ML) and artificial intelligence (AI) models to improve this aspect of the methodology. ML/AI methods may be used to develop a process where the user can directly feed the measured loss-slot rate curves and the model can accurately determine the material properties based on the set of data it is fed, eliminating the need of generating these curves *a priori*.

ACKNOWLEDGMENT

The authors would like to express gratitude to Embry-Riddle Aeronautical University for the financial support of this publication. Additionally, the authors thank Bharat Yelamanchi and Dr. Pedro Cortes of Youngstown State University for the fabrication of YSZ substrate samples. Furthermore, the authors would also like to thank GGB Industries Inc. for their extensive support.

REFERENCES

[1] E. A. Rojas-Nastrucci et al., “Characterization and modeling of K-band coplanar waveguides digitally manufactured using pulsed picosecond laser machining of thick-film conductive paste,” *IEEE Trans. Microw. Theory Techn.*, vol. 65, no. 9, pp. 3180–3187, Sep. 2017.

[2] E. A. Rojas-Nastrucci, A. D. Snider, and T. M. Weller, “Propagation characteristics and modeling of meshed ground coplanar waveguide,” *IEEE Trans. Microw. Theory Techn.*, vol. 64, no. 11, pp. 3460–3468, Nov. 2016.

[3] M. M. Abdin, W. J. D. Johnson, J. Wang, and T. M. Weller, “*W*-Band MMIC chip assembly using laser-enhanced direct print additive manufacturing,” *IEEE Trans. Microw. Theory Techn.*, vol. 69, no. 12, pp. 5381–5392, Dec. 2021.

[4] R. A. Ramirez, E. A. Rojas-Nastrucci, and T. M. Weller, “Laser-assisted additive manufacturing of mm-wave lumped passive elements,” *IEEE Trans. Microw. Theory Techn.*, vol. 66, no. 12, pp. 5462–5471, Dec. 2018.

[5] S. L. Yu and E. A. Rojas-Nastrucci, “Characterization of microdispensed dielectric materials for direct digital manufacturing using coplanar waveguides,” in *Proc. IEEE 20th Wireless Microw. Technol. Conf.*, 2019, pp. 1–3.

[6] K. Alhassoon, Y. Malallah, J. J. Alcantar-Peña, N. Kumar, and A. S. Daryoush, “Broadband RF characterization and extraction of material properties in 3-D printed composite substrates for magnetically tuned circuits,” *IEEE Trans. Microw. Theory Techn.*, vol. 69, no. 3, pp. 1703–1710, Mar. 2021.

[7] V. J. Pynttäri et al., “Application of wide-band material characterization methods to printable electronics,” *IEEE Trans. Electron. Packag. Manuf.*, vol. 33, no. 3, pp. 221–227, Jul. 2010.

[8] Y. Arbaoui, V. Laur, A. Maalouf, and P. Queffelec, “3D printing for microwave: Materials characterization and application in the field of absorbers,” in *Proc. IEEE MTT-S Int. Microw. Symp.*, 2015, pp. 1–3.

[9] B. K. Tehrani, R. A. Bahr, W. Su, B. S. Cook, and M. M. Tentzeris, “E-band characterization of 3D-printed dielectrics for fully-printed millimeter-wave wireless system packaging,” in *Proc. IEEE MTT-S Int. Microw. Symp.*, 2017, pp. 1756–1759.

[10] P. I. Deffenbaugh, R. C. Rumpf, and K. H. Church, “Broadband microwave frequency characterization of 3-D printed materials,” *IEEE Trans. Compon. Packag. Manuf. Technol.*, vol. 3, no. 12, pp. 2147–2155, Dec. 2013.

[11] V. K. S. Yadav, G. Natu, and R. P. Paily, “Fabrication and electrical characterization of printed microresistors of silver nanoparticles using microcantilever-based printing technology,” *IEEE Trans. Compon. Packag. Manuf. Technol.*, vol. 10, no. 1, pp. 57–64, Jan. 2020.

[12] J. Schultz, B. Petrie, C. Bethards, J. Maloney, J. Calzada, and J. Welter, “Flat lens antenna technology for free space material measurements,” in *Proc. Antenna Meas. Techn. Assoc. Symp.*, 2021, pp. 1–6.

[13] M. Janezic and J. Jargon, “Complex permittivity determination from propagation constant measurements,” *IEEE Microw. Guided Wave Lett.*, vol. 9, no. 2, pp. 76–78, Feb. 1999.

[14] W. Eisenstadt and Y. Eo, “S-parameter-based IC interconnect transmission line characterization,” *IEEE Trans. Compon. Packag. Manuf. Technol.*, vol. 15, no. 4, pp. 483–490, Aug. 1992.

[15] C. R. Mejias-Morillo et al., “High-temperature additively manufactured C-band antennas using material jetting of zirconia and microdispending of platinum paste,” *IEEE Open J. Antennas Propag.*, vol. 3, pp. 1289–1301, 2022.

[16] J. Castro, E. Rojas, A. Ross, T. Weller, and J. Wang, “High-K and low-loss thermoplastic composites for fused deposition modeling and their application to 3D-printed ku-band antennas,” in *Proc. IEEE MTT-S Int. Microw. Symp.*, 2016, pp. 1–4.

[17] A. Vyas, V. Rana, D. Gadani, and A. Prajapati, “Cavity perturbation technique for complex permittivity measurement of dielectric materials at X-band microwave frequency,” in *Proc. Int. Conf. Recent Adv. Microw. Theory Appl.*, 2008, pp. 836–838.

[18] J. Castro, E. A. Rojas-Nastrucci, A. Ross, T. M. Weller, and J. Wang, “Fabrication, modeling, and application of ceramic-thermoplastic composites for fused deposition modeling of microwave components,” *IEEE Trans. Microw. Theory Techn.*, vol. 65, no. 6, pp. 2073–2084, Jun. 2017.

[19] A. Verma, Nasimuddin, and H. Singh, “Dielectric loss of multilayer coplanar waveguide using the single layer reduction (SLR) formulation,” in *Asia-Pacific Microw. Conf. Proc.*, 2005, pp. 1–3.

[20] I. Bahl, M. Bozzi, and R. Garg, *Microstrip Lines and Slotlines*, 3rd ed. Norwood, MA, USA: Artech House, 2013.

[21] T. A. Driscoll and L. N. Trefethen, *Schwarz-Christoffel Mapping*, 1st ed. Cambridge, U.K.: Cambridge Univ. Press, 2002.

[22] E. Saff and A. Snider, *Fundamentals of Complex Analysis With Applications to Engineering and Science*, 3rd ed. New York, NY, USA: Pearson, 2017.

[23] MG Chemicals, “Copper clad boards 500 series technical data sheet,” Apr. 2022. [Online]. Available: https://www.mgchemicals.com/downloads/tds/tds-500-series.pdf

SENG LOONG YU (Student Member, IEEE) received the B.S. degree in electrical engineering from the University of South Florida, Tampa, FL, USA, in 2015, the M.S. degree in electrical engineering from San Jose State University, San Jose, CA, USA, in 2017, and the Ph.D. degree in electrical engineering and computer science from Embry-Riddle Aeronautical University, Daytona Beach, FL, USA, in 2022. During his time with the University of South Florida, he was an Undergraduate Research Assistant with the Center for Wireless and Microwave Information Systems Lab. While with San Jose State University, he studied CMOS RF and analog IC design and was a Lab Instructor of the undergraduate electronics course. His Ph.D. research involves advanced manufacturing and dielectric characterization methods for high-temperature mm-wave antennas in ERAU’s Wireless Devices and Electromagnetics Laboratory. He also worked on revamping the RF/microwave course and taught the lab sessions. He is currently a Senior Design Engineer with Qorvo, Inc., working on BAW filter design in highly integrated RF front-end modules to meet customer specifications.

EDUARDO A. ROJAS-NASTRUCCI (Member, IEEE) received the M.S. and Ph.D. degrees in electrical engineering from the University of South Florida, Tampa, FL, USA, in 2014 and 2017, respectively. He joined the Embry-Riddle Aeronautical University, Daytona Beach, FL, USA, in 2017, where he is an Associate Professor. His research interests include microwave/mm-wave circuits and antenna applications of additive manufacturing and wireless sensing for harsh environments, in the context of aviation and space systems. He is the co-director of ERAU’s Wireless Devices and Electromagnetics Laboratory. He was the recipient of the CAREER Award from the National Science Foundation in 2019, the 2022 Jet Propulsion Laboratory Faculty Fellowship, the 2020 Most Promising Engineer Award, Ph.D. Education category, from the Great Minds in Stem organization, and the ERAU’s 2021 Abas Sivjee Outstanding Research Award. He has more than 50 peer-reviewed publications and seven U.S. patents. He is a member of the IEEE MTT-S Technical Committees 4, 26, and 29; and the RTCA SC-236 Committee for Standards for Wireless Avionics Intra-Communication System within 4200-4400 MHz. He was the General Conference Chair of the 2022 IEEE Wireless and Microwave Technology Conference.